









Measurement of the $^{238}\text{U}(n, f)$ prompt fission neutron spectrum from 10 keV to 10 MeV induced by neutrons with 1.5–20 MeV energy

K. J. Kelly ^{1,*}, M. Devlin ¹, J. M. O'Donnell,¹ D. Neudecker,¹ A. E. Lovell ¹, R. C. Haight,¹ C. Y. Wu ², R. Henderson,² E. A. Bennett ¹, T. Kawano ¹, J. L. Ullmann,¹ N. Fotiades ¹, J. Henderson,² S. M. Mosby,¹ T. N. Taddeucci,¹ P. Talou,¹ M. C. White ¹, J. A. Gomez,¹ and H. Y. Lee¹

¹Los Alamos National Laboratory, Los Alamos, New Mexico 87545, USA

²Lawrence Livermore National Laboratory, Livermore, California 94550, USA



(Received 13 February 2023; revised 6 June 2023; accepted 24 July 2023; published 14 August 2023)

With the recent emergence of fast nuclear reactors, there has been a corresponding increasing interest in ^{238}U -related nuclear data. However, while existing literature data span much of the energy ranges of interest for the prompt fission neutron spectrum (PFNS) for neutron-induced fission of ^{238}U , most literature data sets are highly correlated, and thus new, independent measurements of this quantity are needed. In this work, we report the results of a new measurement of the ^{238}U PFNS at the Los Alamos Neutron Science Center for incident neutron energies from 1.5–20.0 MeV, and outgoing neutron energies of 0.01–10.0 MeV. With some notable exceptions, the present results generally agree with existing literature data, especially with regard to features relating to multichance fission and pre-equilibrium features in the PFNS, thus adding confidence to existing nuclear data evaluations and filling in gaps of knowledge at previously unmeasured incident neutron energies. This result is the third in a series of PFNS measurements by the Chi-Nu collaboration now spanning all three major actinides, ^{239}Pu , ^{235}U , and ^{238}U . Thus, for the first time, we report reliable experimental PFNS ratios and average PFNS energy comparisons for measurements of all three of these isotopes including accurate correlations between the different, but correlated experiments.

DOI: [10.1103/PhysRevC.108.024603](https://doi.org/10.1103/PhysRevC.108.024603)

I. INTRODUCTION

Monte Carlo simulations are utilized for performance and safety calculations of new nuclear reactor designs (see, e.g., Refs. [1,2]). Light water (i.e., lower neutron energy) reactors are largely insensitive to the neutron-induced fission of ^{238}U owing to the fission threshold of approximately 1.5 MeV [3]. However, the recent emergence of fast (i.e., higher neutron energy) sodium-cooled reactors has brought deficiencies in nuclear data related to ^{238}U near the top of lists of current nuclear data needs (see Refs. [1,4] and references therein). Thus, the energy spectrum of neutrons emitted from neutron-induced fission [i.e., the prompt fission neutron spectrum (PFNS)] of ^{238}U is of fundamental importance for understanding the distribution of neutron energies available for reactions in these fast reactor systems. Along with the average number of emitted neutrons from fission and the fission cross section, the PFNS is one of the major fission quantities required for criticality calculations, and of these three is has by far the highest uncertainty.

Compared with other actinides, ^{238}U has a reasonably broad coverage of incident (E_n^{inc}) and outgoing (E_n^{out}) neutron energies from historic experimental data sets. See Table I for a list of all experiments and the incident energies measured. However, upon further investigation two important features of

these data become clear: (1) As stated in Table VI of Ref. [5], the results of Refs. [6–15] were all reported with incomplete uncertainty quantification, and (2) the measurements of Refs. [8–13] are all highly correlated with each other in that the author lists are usually almost identical, the analysis techniques applied are generally consistent, and the experimental facility and equipment are similar if not identical. Thus, despite this wide E_n^{inc} coverage range, it is possible that there exists a systematic bias in the measurements of Refs. [8–13], which make up the vast majority of literature data on the ^{238}U PFNS. Furthermore, while data of Ethvignot *et al.* [16] are uncorrelated with Refs. [8–13] and are available for a continuous range of $E_n^{\text{inc}} = 1.59\text{--}200$ MeV, these data are reported only as average neutron energies for the limited outgoing neutron energy of $E_n^{\text{out}} = 0.65\text{--}7.5$ MeV and as less reliable Watt [17] function fits to their data. We also note the existence of data for $E_n^{\text{inc}} = 5.0\text{--}6.0$ and $7.0\text{--}8.0$ MeV in Ref. [18]. These data were stated to be preliminary in Ref. [18], and thus are not shown in this work, though no subsequent results have been published from these measurements. Lastly, the data of Wen *et al.* [19] and Sardet *et al.* [20] are also uncorrelated with Refs. [8–13], respectively, though the former appears to contain a significant systematic error.

In this work, we report on measurements of the ^{238}U PFNS using the Chi-Nu experimental setup at Los Alamos National Laboratory. By design, each Chi-Nu experiment for a specific isotope is nearly identical to that of each other isotope, with the exception of slight differences in the target characteristics

*Corresponding author: kkelly@lanl.gov

TABLE I. Summary of literature measurements of the $^{238}\text{U}(n, f)$ PFNS measurements.

| Ref. | First author | E_n^{inc} (MeV) |
|---------|-------------------|--------------------------|
| [6] | Baba (1989) | 2.0 |
| [7] | Desai (2015) | 2.0, 2.5, 3.0 |
| [8] | Kornilov (1980) | 6.01, 7.02, 8.01, 8.94 |
| [9,10] | Boikov (1991) | 2.9, 14.7 |
| [11] | Trufanov (2001) | 5.0, 13.2 |
| [12] | Lovchikova (2004) | 6.0, 7.0 |
| [13] | Smirenkin (1996) | 16.0, 17.7 |
| [14,15] | Baryba (1977) | 14.3 |
| [16] | Ethvignot (2003) | 1.59–200 |
| [19] | Wen (2016) | 2.8 |
| [20] | Sardet (2013) | 5.2 |

and random variations in experimental setup. Thus, given that two previous measurements have been published in highly detailed Physical Review C papers [21,22] along with a series of additional publications describing further details of the analysis and experimental data [23–31], this paper highlights only the most fundamental details of the Chi-Nu ^{238}U PFNS experiment reported here. Specifically, we focus on highlighting differences in the experiment and acquired data, as well as some studies of systematics between this ^{238}U data set and previous ^{239}Pu [21] and ^{235}U [22] results. Details omitted from this article can be assumed to be identical to the details given in Refs. [21] and [22]. We describe the experimental setup in Sec. II, the data analysis procedures in Sec. III, and results, including comparisons of the present ^{238}U results with those of ^{239}Pu [21] and ^{235}U [22] in Sec. IV. Concluding remarks are given in Sec. V.

II. EXPERIMENTAL SETUP

Measurements were carried out at the Weapons Neutron Research (WNR) facility at the Los Alamos Neutron Science Center (LANSCE) [32]. The WNR incident neutron beam is a pulsed white neutron source, spanning a typically useful range of 0.7–20 or 30 MeV with some experiments reporting data at higher energies. The incident neutron beam is generated from spallation of 800 MeV protons incident on a tungsten target, with a signal referred to as the t_0 signal being generated just before the spallation reactions. For these experiments, neutrons traveling at 15° to the left of the incident proton beam direction were collimated before impinging on a parallel-plate avalanche counter (PPAC) target [33] 21.5 m from the target. This target chamber contains ten double-sided 99.959% pure ^{238}U deposits approximately 4 cm in diameter each, totaling approximately 70 mg of total target material. The remaining composition of the target material consists of 0.040% ^{235}U and 0.005% ^{234}U , and contributions from these contaminants to the observed neutron spectra are negligible. These PPAC targets provide a time resolution for the fission time, t_f , of less than 1.0 ns, though no fragment mass or angular information is provided by the PPAC itself.

As was described in more detail in Refs. [21,22], these detectors also measure α particles spontaneously emitted from ^{238}U which overlap with signals from the fission frag-

ments of interest for a portion of the spectrum. This α background contributes to random-coincidence backgrounds (see Sec. III B) and was removed during data analysis. This α background for this work was approximately a factor of 10^5 reduced compared with the ^{239}Pu measurement in Ref. [21], and therefore was not a concern. Approximately 99% of detected fission events were accepted for the data analysis described in subsequent sections. The efficiency for detecting fragments in the PPAC targets used in Chi-Nu experiments changes with the fragment emission angle, which is impacted by beam kinematics, intrinsic fragment anisotropy, and other effects. As described in Sec. III C, these effects were taken into account using Monte Carlo calculations combined with Hauser-Feshbach fission model calculations. The potential for distortion of the measured PFNS due to these effects was quantified with an identical process to that of Refs. [21,22], and resulted in a systematic uncertainty on the final results.

The incident neutron energy, E_n^{inc} , was measured via the $t_f - t_0$ time difference, defined to be the time of flight of incident neutrons from the source to the PPAC corrected by a constant related to cable lengths. The sub-nanosecond time resolution for incident neutron times of flight as short as 281.385 ns relative to the corresponding γ -ray transit time results in incident-neutron energy uncertainties $<0.3\%$, and so these uncertainties were safely ignored.

Neutrons were detected in one of two detector arrays, each of which is run in a separate experiment. Neutrons with outgoing neutron energy, E_n^{out} , from 0.01–1.59 MeV are measured with a 22-detector Li-glass array [25,34] each nominally 0.400(5) m from the PPAC center, while those with $E_n^{\text{out}} = 0.89$ –10.0 MeV were detected with a 54-detector liquid scintillator array each nominally 1.020(5) m from PPAC center [35,36]. For both experiments, a fission-neutron time coincidence window of $t_f - 150$ ns, and $t_f + 350$ ns was enforced in a postprocessing analysis of the asynchronously collected data, with neutrons detected at a time t_n . The E_n^{out} for each neutron was assigned based on the $t_n - t_f$ time difference. Li-glass coincidences with PPAC signals yielded a $1\text{-}\sigma$ time resolution of 1.11(1) ns, while those with liquid scintillators displayed a 1.08(1) ns resolution, also at $1\text{-}\sigma$. This data acquisition and signal processing analysis produced spectra such as that shown in Fig. 1, which are amenable to the analysis details provided in the next section. Note in Fig. 1 the sharp reduction of counts near $E_n^{\text{inc}} = 1.5$ MeV because of the threshold for fission in this nucleus. The negligible amount of data below this energy also adds confidence to the lack of ^{235}U contamination in the present data, which would produce fission-correlated neutron detections below this energy. Lastly, the diagonal feature observed from $(E_n^{\text{inc}}, E_n^{\text{out}}) \approx (7.0\text{ MeV}, 0.8\text{ MeV})$ – $(12.0\text{ MeV}, 6.0\text{ MeV})$ is a direct observation of the high impact of the second-chance fission process on these data (see Sec. IV).

III. DATA ANALYSIS

A. Signal processing

To initially eliminate signals from the data that do not correspond to the fission-correlated neutron data of interest, PPAC spectra were cut at low pulse integrals to remove as

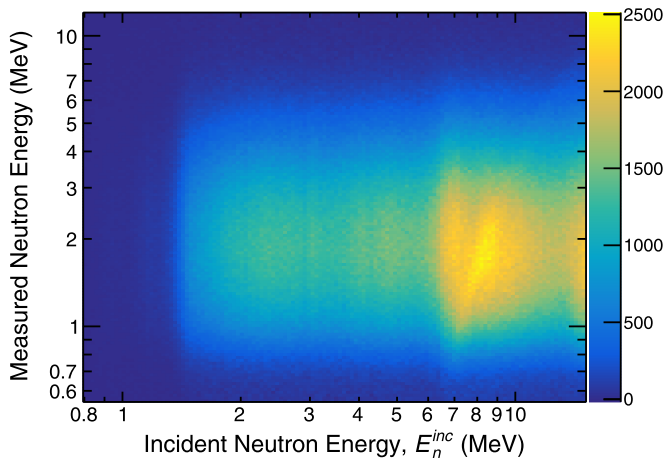


FIG. 1. An example spectrum of outgoing versus incident neutron energy for the liquid scintillator data obtained for this work summed over all detection angles, and after random-coincidence background subtraction. The neutron energy on the y axis is the measured outgoing neutron energy from time of flight, before conversion to a PFNS result, and counts along the z axis refer to counts in each logarithmically spaced bin before corrections for varying bin size. See the text for a discussion of features in this spectrum.

many α particles as possible. Also, γ rays were eliminated from liquid scintillator results using pulse shape discrimination (PSD) as well as expected kinematics of neutron emission. Li-glass detectors do not have PSD capabilities, but kinematics alone were sufficient to remove γ rays from Li-glass data, as was confirmed by data collected using a Li-glass detector enriched in ^7Li , as opposed to ^6Li . Additional cuts were placed on the acquired signals to reduce noise and signal reflections in the cables, and corrections for walk (i.e., a trend of altered detection time observed as a function of the magnitude of a given pulse [37]) were made to all detectors as needed after the application of constant fraction discrimination to the timing of all signals. There was no need to correct for issues relating to dead time in these measurements.

Timing calibrations were made such that γ rays emitted from the proton-induced reactions in the tungsten spallation target were aligned at $t_f - t_0 = 0$ ns, which is observed in the PPAC targets as a γ -induced fission peak. Incident neutron energies were calculated relativistically with respect to the transit time of γ rays down the ≈ 21.5 m flight path. Similarly, neutron detector signals were aligned in time such that the γ rays from fission (better observed without PSD cuts in the liquid scintillators) were observed at $t_n - t_f = 0$ ns, and emitted neutron energies were assigned based on the time of flight relative to the transit time for a γ rays traveling to the neutron detectors. The binning for outgoing neutrons was chosen to be a logarithmic 20 bins per decade in an effort to (a) obtain sufficient statistics in each energy bin [21], and (b) define a binning that can be easily made consistent between different detector types and between the PFNS results of all actinides measured during the Chi-Nu project, the latter of which is essential for, e.g., PFNS ratios like those shown in Sec. IV E.

B. Random-coincidence backgrounds

Random (or chance) coincidences between acquired signals are typically a dominant contributor to backgrounds in data from coincidence measurements. For example, an α particle detected in a PPAC could be accidentally measured to be in coincidence with a neutron from fission; a true fission event could be detected in coincidence with a neutron not originating from fission; or a true fission event and a PFNS neutron not originating from the same fission event could be accidentally measured to be in coincidence with each other. All of these kinds of events are part of the measured data, but a method to identify the amount of data corresponding to all varieties of random-coincidence detection must be applied to obtain the foreground coincidence data.

The methods of Ref. [26] were employed for these measurements, and all other Chi-Nu PFNS measurements. This method uses the pre-coincidence, in-beam data to define the probability of randomly detecting uncorrelated fission and neutron events in coincidence with each other as a function of time and per observed t_0 signal, which is then scaled by the total number of observed t_0 signals to obtain the random-coincidence background spectrum. Since this method uses the pre-coincidence data, which have much higher statistics than the post-coincidence data, the random-coincidence background has orders of magnitude smaller statistical uncertainty than the post-coincidence data ultimately used to extract the PFNS.

Recently, the potential for systematic errors in this method was explored in Ref. [31], and a method for correcting the background for any deficiencies related to rate changes over the course of an experiment, correlations between detection rates, or any other means of introducing an error in the background spectrum. The method for correcting the background was defined earlier in Ref. [21], and was applied to both previous Chi-Nu measurements [21,22], but the precise origin of the need for these corrections was not fully explored or published until Ref. [31]. See Refs. [26,31] for more details on this method.

C. MCNP®-based corrections

Chi-Nu PFNS experiments are fundamentally different than nearly every other measurement of a neutron-induced PFNS in that the corrections to the data for neutron scattering in the environment, neutron attenuation in air, nuclear reactions in the detectors, and detector efficiency are all determined using highly detailed MCNP®,¹ [38,39] simulations developed over the decade leading up to the first results from the Chi-Nu project [25,27]. As such, the environment and neutron response characteristics of these simulations are well

¹MCNP6® and Monte Carlo N-Particle® are registered trademarks owned by Triad National Security, LLC, manager and operator of Los Alamos National Laboratory. Any third party use of such registered marks should be properly attributed to Triad National Security, LLC, including the use of the designation as appropriate. For the purposes of visual clarity, the registered trademark symbol is assumed for all references to MCNP within the remainder of this paper.

trusted and vetted. With the exception of measurements of the ^{252}Cf spontaneous fission PFNS and very few other cases, in effectively all other neutron-induced PFNS measurements the neutron detector efficiencies are measured relative to the ^{252}Cf spontaneous fission PFNS, and this one-dimensional (1D) efficiency is applied to the measured spectrum (see Ref. [5] and references therein). For Chi-Nu PFNS results, the distortion of a series of representative template PFNS input spectra through all of the above-mentioned effects is calculated, and the average ratio of the input spectra to the observed output spectra from the simulation (as measured with neutron time of flight) is used to convert the experimental data to the PFNS shape. Simulated data were resolved and aligned according to experimentally measured pulse-integral and time resolutions. Note that only this single averaged ratio is applied to each incident neutron energy bin reported for the $^{238}\text{U}(n, f)$ in this work, which produces a correlation between the results of each incident neutron energy.

Similar to the choice of utilizing the ^{252}Cf spontaneous fission PFNS to correct data for neutron efficiency and scattering effects, the choice of the template spectra for this MCNP-based approach impacts the results of this work. However, a primary benefit of the method applied to Chi-Nu PFNS results is that a rigorously defined covariance for the accuracy, or applicability, of this “ratio-of-ratios” correction to the data can be derived from variations in the simulated input-output ratios. The generation of a covariance defining the potential error of the method (as opposed to the reference nuclear data quantities) is not possible with traditional measurements using ^{252}Cf to measure either the efficiency or as a direct ratio reference spectrum (both of which are equivalent); the covariance corresponding to the method of measuring relative to ^{252}Cf is the covariance of the ^{252}Cf reference itself. This systematic uncertainty should then be added to the potential errors in the method itself, though the errors in the method are not calculable without accurate simulations or additional measurements.

In addition to the fundamentally important corrections for environmental scattering and detector efficiency, MCNP simulations were also used to assess the impact of the angular dependence of the PPAC fragment detector efficiency, the angular anisotropy of fission fragment emission, and kinematics of the fission reaction followed by neutron emission. More specifically, it is the combination of these three effects that can cause potential errors in the PFNS at any specific emission angle. To explore these effects, we used CGMF [40] calculations integrated with MCNP simulations to infer the observed E_n^{out} spectrum as a function of neutron detection angle, and of fragment emission angle. While this correlation is complicated to describe and quantify given that the PPAC targets used for this work do not yield any angular or mass information about the fission fragments, this source of systematic uncertainty was not a major source of systematic uncertainty in previous Chi-Nu measurements [21,22]. However, the anisotropy of fragments emitted from the neutron-induced fission of ^{238}U is significantly stronger compared with ^{239}Pu and ^{235}U [41–44]. Thus, following the same procedures, we determine a systematic uncertainty of roughly 0.4–2.0 % on average for the present measurement, as opposed to roughly 0.05–1.0 % or

lower on average for previous Chi-Nu measurements. See the discussion in the next section for more details on the shape of this uncertainty source.

D. Production of the final PFNS results and covariances

Following extraction of the PFNS from both the Li-glass and liquid scintillator data sets, the two separate measurements were combined with the requirement that the area in the overlap region of outgoing fission neutrons in the range 0.89–1.59 MeV is the same. The covariance for the combined data set includes statistical uncertainties on the data, background, and MCNP simulations, along with systematic uncertainties from the background, ratio-of-ratios method of PFNS extraction, input nuclear physics into MCNP simulations, post-processing parameters used to match MCNP simulations to data, corrections for fragment angular distributions and PPAC fragment detection efficiencies, and fragment-neutron kinematics. The combination of these two data sets initially amounts to a scaling factor for each data set. The combined shape was subsequently normalized to unit area, including full covariance propagation through the normalization procedure, in order to properly report a PFNS shape data set [30,48]. The neutron energy uncertainties on the present results derived from time and distance resolutions are included as x -axis uncertainties in the following section, and are not reflected in Fig. 2. Note also that below $E_n^{\text{out}} \approx 0.07$ MeV statistical uncertainties dominate the total uncertainty owing the high background in these regions, which results in large fluctuations of the total uncertainty.

Notable compared to previous Chi-Nu PFNS results is the fact that the correction for wraparound (i.e., incident neutron contamination from neighboring beam pulses) is not needed for ^{238}U PFNS results because of the fission threshold of approximately 1–2 MeV for ^{238}U [3]. In reality, fission can occur below this threshold, but the probability of fission occurring closely below this threshold is a factor of approximately 20 or more less likely than just above this threshold. The magnitude of this correction is further reduced by the fact that the incident neutron flux from the previous pulse inducing the wraparound contamination is typically at least an order of magnitude lower than the most recent (principal) neutron pulse, and the correction is usually only on the order of a few percent even when it is important. Thus, the reduction in fission cross section in the wraparound region renders this correction negligible for this data set. The contributions from various sources of uncertainty for the normalized ^{238}U shape for $E_n^{\text{inc}} = 2.0$ –3.0 MeV are shown in Fig. 2.

IV. RESULTS

In the following sections experimental results are reported with regard to PFNS shape in Secs. IV A–IV C, average neutron energy of the PFNS in Sec. IV D, and trends across consistent Chi-Nu measurements of the ^{239}Pu , ^{235}U , and ^{238}U PFNS distributions in Sec. IV E. Shape results are split into groups of consistent paths available to a fission event, which changes with E_n^{inc} . PFNS shape results for fission proceeding via neutron capture directly followed by fission of a ^{239}U

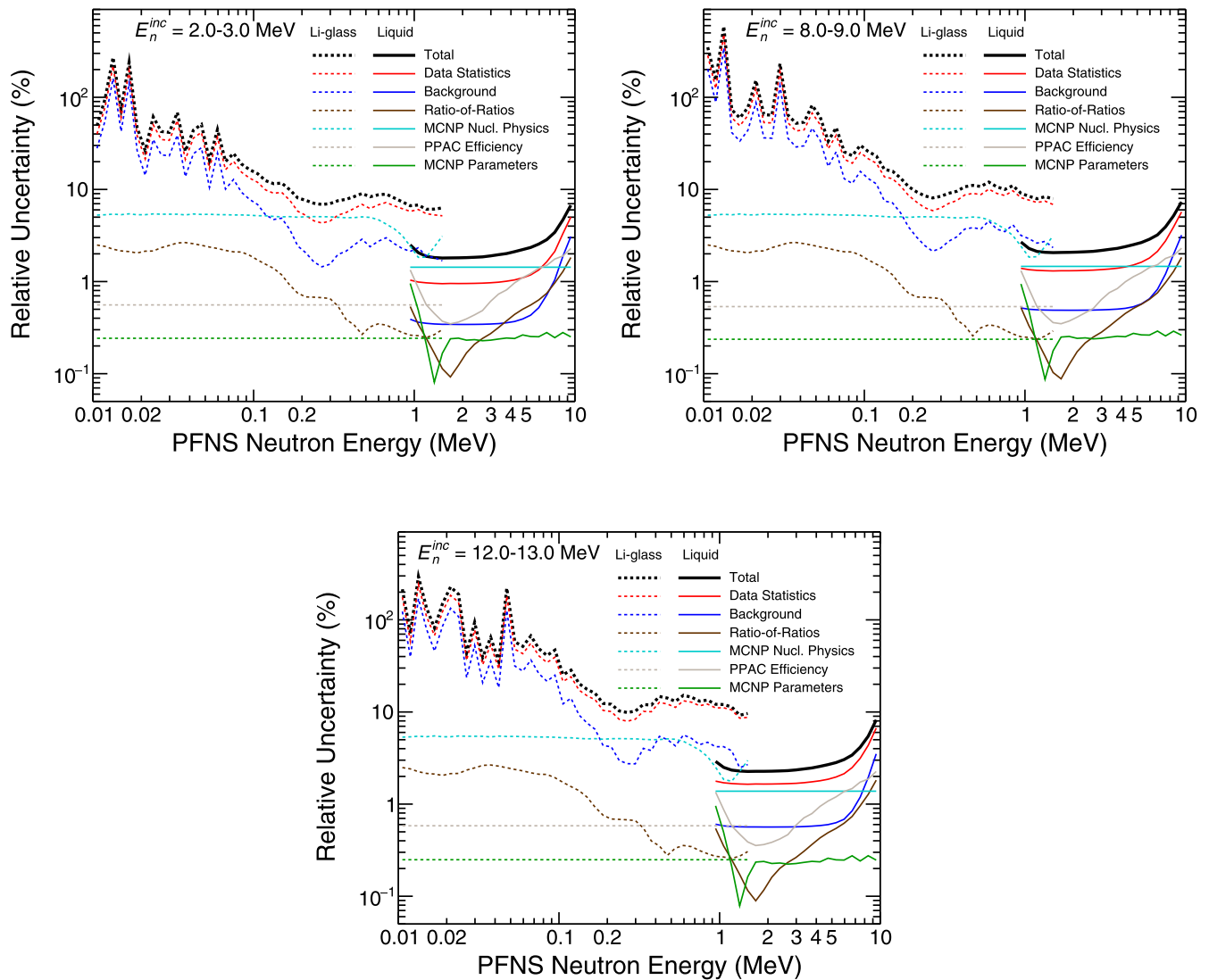


FIG. 2. The relative uncertainty from all non-negligible sources of uncertainty in the present data set for the final PFNS results from (a) $E_n^{\text{inc}} = 2.0\text{--}3.0$ MeV, (b) $8.0\text{--}9.0$, and (c) $12.0\text{--}13.0$ MeV. These E_n^{inc} ranges correspond to one range present in each of Secs. IV A, IV B, and IV C.

nucleus (termed first-chance fission) are shown in Sec. IV A. Results in Sec. IV B correspond to a combination of first- and second-chance fission, with the latter allowing a neutron to boil off of the ^{239}U compound nucleus before a ^{238}U nucleus fissions. Section IV C then shows results from a combination of first-, second-, and third-chance fission (i.e., emission of two neutrons before a ^{237}U nucleus fissions), as well as the pre-equilibrium neutron emission process preceding fission in which a compound ^{239}U nucleus is never formed and a ^{238}U nucleus fissions. These varieties of fission events produce distinct PFNS shapes, but are experimentally indistinguishable on an event-by-event basis. Thus, the results are necessarily a combination of all available processes.

A. PFNS results from $E_n^{\text{inc}} = 1.0\text{--}5.0$ MeV

Since the $^{238}\text{U}(n, f)$ cross section drops dramatically below $E_n^{\text{inc}} \approx 1.5$ MeV, we report data only down to $E_n^{\text{inc}} =$

1.5 MeV as opposed to 1.0 MeV for the Chi-Nu ^{239}Pu and ^{235}U PFNS results. Furthermore, the statistical variation of the Li-glass data collected for these results in the overlap region between liquid scintillator and Li-glass data made a reliable relative normalization between these data sets not possible for the $E_n^{\text{inc}} = 1.5\text{--}2.0$ MeV range. Therefore, we only report liquid scintillator data for the $E_n^{\text{inc}} = 1.5\text{--}2.0$ MeV energy range shown in Fig. 3(a).

For the incident neutron energy range $E_n^{\text{inc}} = 2.0\text{--}3.0$ MeV there exist literature data from four authors for comparison: Desai *et al.* [7], Baba *et al.* [6], Boikov *et al.* [9], and Wen *et al.* [19]. Desai *et al.* also reported three data sets at $E_n^{\text{inc}} = 2.0$, 2.5, and 3.0 MeV, shown in Figs. 3(a), 3(b), and 3(c), respectively. While the data of Wen *et al.* [19] were collected using a unique emulsion technique, these data are not shown for comparison here because the shape of their results strongly disagrees with all nuclear data evaluations, literature data, and the present results by more than 5σ for most of the E_n^{out}

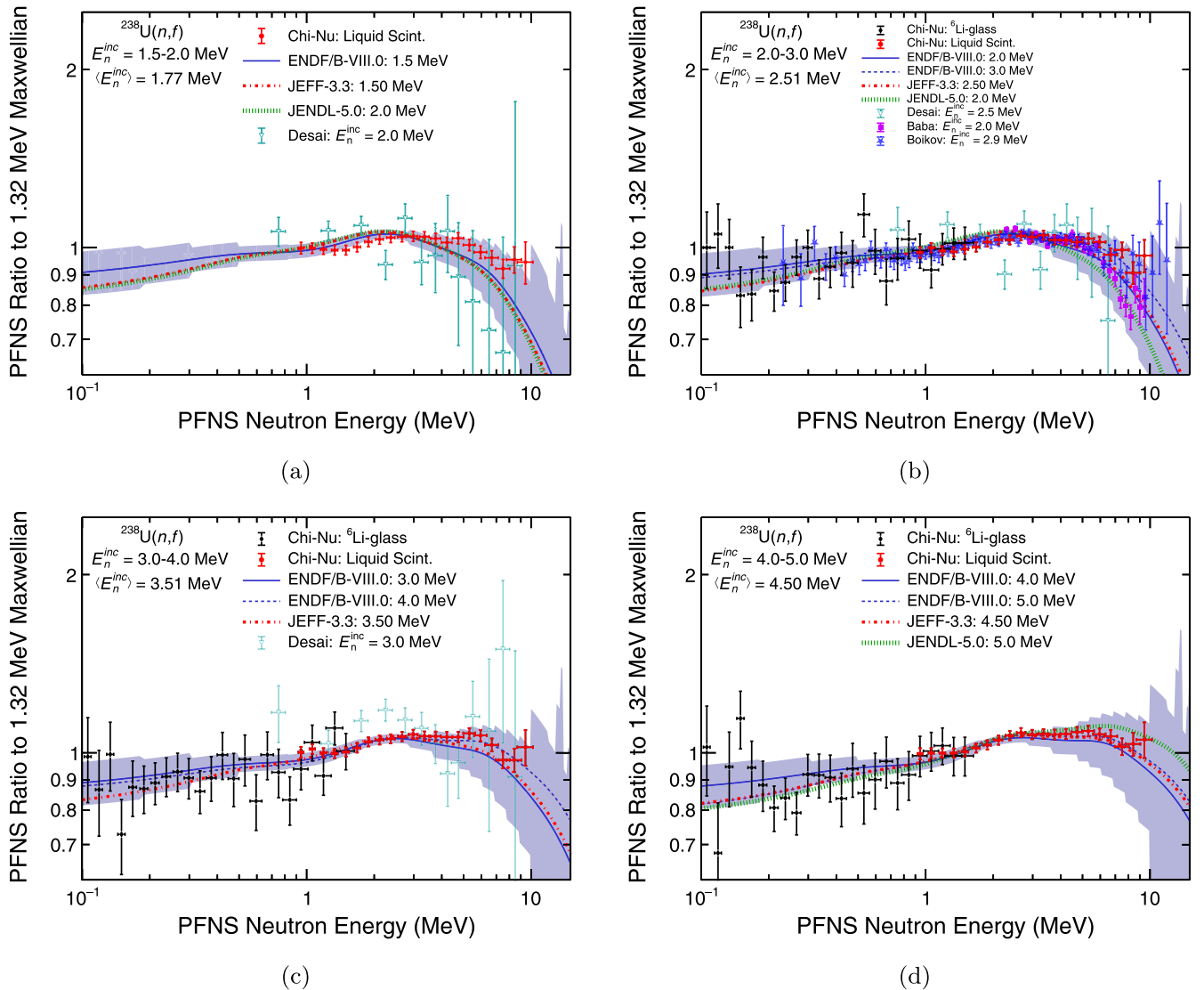


FIG. 3. The present results for Li-glass (black diamonds) and liquid scintillator (red circles) data are shown for (a) $E_n^{inc} = 1.5\text{--}2.0$, (b) $2.0\text{--}3.0$, (c) $3.0\text{--}4.0$, and (d) $4.0\text{--}5.0$ MeV, corresponding to average incident neutron energy, $\langle E_n^{inc} \rangle$, values of 1.77, 2.51, 3.51, and 4.50 MeV, respectively. ENDF/B-VIII.0 [3] evaluations are shown as solid and dashed blue lines, JEFF-3.3 [45] as the dash-dotted red lines, and JENDL-5.0 [46] as dotted green lines. The shaded blue region corresponds to the uncertainty of the lower E_n^{inc} ENDF/BB-VIII.0 evaluation on each plot. All other evaluation uncertainties can be assumed to be similar. Literature data are plotted as compiled in EXFOR [47]. All data are shown as a ratio to a 1.32 MeV Maxwellian.

range reported in that work. All remaining authors compared within this E_n^{inc} range [6,7,9] measured the PFNS at a single angle with respect to the orientation of the ^{238}U target, with Desai utilizing two detectors at the same polar angle, and Boikov and Baba employing a single detector in a highly shielded environment. Bearing in mind the difference in E_n^{inc} for each of these measurements as well as the range of E_n^{inc} measured for the present results, all data agree quite well within uncertainties, though the large total uncertainties for the Desai *et al.* data make detailed comparisons difficult. For $E_n^{inc} = 1.5\text{--}2.0$ MeV, our results suggest a slight increase to the evaluated PFNS at higher energies, but agreement above that incident neutron energy appears generally good for the ENDF/B-VIII.0 [3], JEFF-3.3 [45], and JENDL-5.0 [46] libraries. Note that JENDL-5.0 is identical to JENDL-4.0 for

the ^{238}U PFNS, and the evaluated E_n^{inc} grid does not include any energy points between $E_n^{inc} = 2.0$ and 5.0 MeV.

B. PFNS results from $E_n^{inc} = 5.0\text{--}10.0$ MeV

The threshold for second-chance fission is crossed in the $E_n^{inc} = 5.0\text{--}10.0$ MeV range, from which we expect to observe a low- E_n^{out} excess in the PFNS. Literature data from Sardet *et al.* [20], Trufanov *et al.* [11] at $E_n^{inc} = 5.0$ MeV, Lovchikova *et al.* [12] at $E_n^{inc} = 6.0$ and 7.0 MeV, and Kornilov *et al.* [8] at $E_n^{inc} = 6.01, 7.02, 8.01,$ and 8.94 MeV are all available for comparison in this range as well. The data of Trufanov *et al.* in Fig. 4(a) have a markedly different shape compared with the present results and all plotted nuclear data evaluations above $E_n^{out} \approx 6.0$ MeV; the Trufanov data tend to be notably

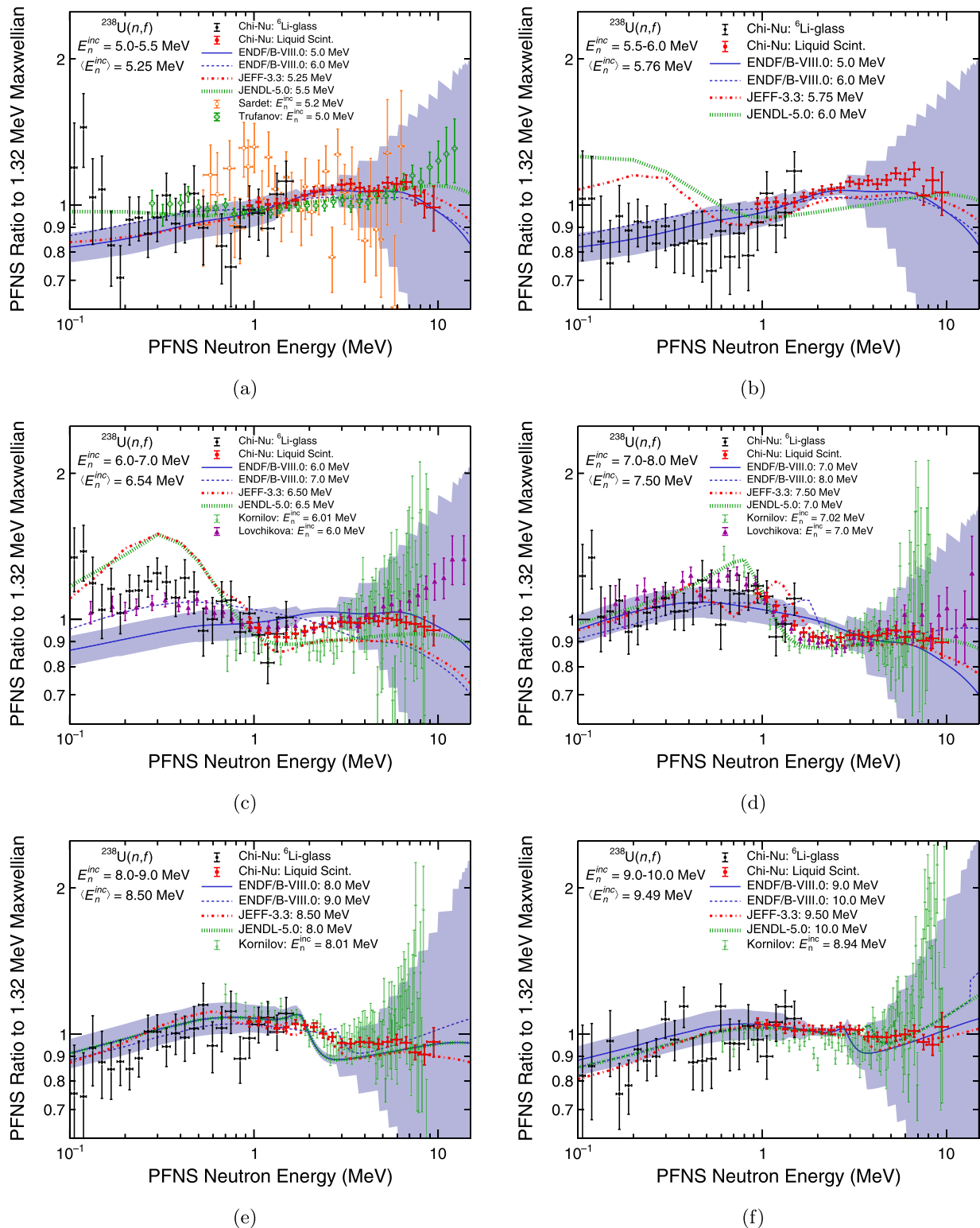


FIG. 4. The present results for Li-glass (black diamonds) and liquid scintillator (red circles) data are shown for (a) $E_n^{\text{inc}} = 5.0\text{--}5.5$, (b) $5.5\text{--}6.0$, (c) $6.0\text{--}7.0$, (d) $7.0\text{--}8.0$ MeV, (e) $8.0\text{--}9.0$, and (f) $9.0\text{--}10.0$ MeV, corresponding to average incident neutron energy, $\langle E_n^{\text{inc}} \rangle$, values of 5.25, 5.76, 6.54, 7.50, 8.50, and 9.49 MeV, respectively. ENDF/B-VIII.0 [3] evaluations are shown as solid and dashed blue lines, JEFF-3.3 [45] as the dash-dotted red lines, and JENDL-5.0 [46] as dotted green lines. The shaded blue region corresponds to the uncertainty of the lower E_n^{inc} ENDF/BB-VIII.0 evaluation on each plot. All other evaluation uncertainties can be assumed to be similar. Literature data are plotted as compiled in EXFOR [47]. All data are shown as a ratio to a 1.32 MeV Maxwellian distribution.

higher at high E_n^{out} values, though their shape agrees well with the JENDL-5.0 evaluation at lower E_n^{out} values. This same figure, the data of Sardet *et al.* generally have lower statistical precision, and thus comparisons are not informative. In Fig. 4(b), our data appear to suggest a slightly later (higher E_n^{inc}) onset of second-chance fission compared with the results of the JEFF-3.3 and JENDL-5.0 evaluations, both of which show a clear low- E_n^{out} excess below $E_n^{\text{out}} = 6.0$ MeV, whereas the present results and the ENDF/B-VIII.0 evaluation do not show much of this feature in this energy range.

In Figs. 4(c) and 4(d) the expected low- E_n^{out} excess becomes clear in the present results, and agrees very well with the PFNS shapes observed by Kornilov *et al.* and Lovchikova *et al.* in the $E_n^{\text{out}} \approx 0.6$ –3.0 MeV range. Similar to the data from Trufanov *et al.*, the results of Lovchikova *et al.* in Fig. 4(c) trend higher than the present data above $E_n^{\text{out}} \approx 6.0$ MeV, though the data of Lovchikova *et al.* are in agreement within uncertainties of the present results in Fig. 4(d). The data of Kornilov *et al.* agree with the present results at all four incident energies they report shown in Figs. 4(c)–4(f) within their uncertainties. While the second-chance fission features of the present results seem to agree well with JENDL-5.0 in Fig. 4(d) and with all evaluations in Figs. 4(e)–4(f) (where all evaluation tend to agree with each other as well), no single evaluation seems to agree with the data consistently through Figs. 4(a)–4(d).

C. PFNS results from $E_n^{\text{inc}} = 10.0$ –20.0 MeV

Above $E_n^{\text{inc}} = 10.0$ MeV we approach thresholds for both third-chance fission and pre-equilibrium neutron emission processes. Literature data from Trufanov *et al.* [11] at $E_n^{\text{inc}} = 13.2$ MeV, Baryba *et al.* [15] at $E_n^{\text{inc}} = 14.3$ MeV, Boikov *et al.* [9] at $E_n^{\text{inc}} = 14.7$ MeV, and Smirenkin *et al.* [13] at $E_n^{\text{inc}} = 16.0$ and 17.7 MeV are available in this range. Similar to the other correlated experiments (see Sec. I), a single neutron detector was used in a highly-shielded environment for all of these measurements. This fact becomes particularly important at higher E_n^{inc} ranges because the pre-equilibrium neutron emission process is known to produce a neutron angular distribution peak at forward angles relative to the incident neutron beam. Thus, it is difficult to obtain the correct angle-integrated PFNS from a single neutron detection angle. The most obvious feature from this pre-equilibrium emission process is a peak in the PFNS at high outgoing energies relative to a Maxwellian distribution, though neutrons with lower energies are also produced in this process.

Results for $E_n^{\text{inc}} = 10.0$ –15.0 MeV and 15.0–20.0 MeV are shown in Figs. 5(a)–5(e) and 6(a)–6(e), respectively. From $E_n^{\text{inc}} = 10.0$ –13.0 MeV in Figs. 5(a)–5(c), the emergence of neutrons from the pre-equilibrium process is observed as the peak in the PFNS relative to a Maxwellian starting at $E_n^{\text{out}} \approx 4.0$ –5.0 MeV in Fig. 5(a) and increasing in both E_n^{out} and magnitude (as a ratio to a Maxwellian distribution) as E_n^{inc} increases. When comparing the present results to evaluations, especially for this pre-equilibrium peak, it is important to keep in mind that while the present results are reported over a range of incident neutron energies, the evaluations are reported at single incident neutron energies. Thus, it is

expected that, for example, the width of the pre-equilibrium peak in the present results is wider than for an evaluation at any individual E_n^{inc} value in the plotted range, and this generally appears to be the case for all evaluations shown, though the JEFF-3.3 evaluation appears to agree with the observed centroid of this peak perhaps better than the ENDF/B-VIII.0 or JENDL-5.0 evaluations.

Third-chance fission PFNS features start to appear in Figs. 5(d) and 5(e) as another low- E_n^{out} excess, though the magnitude of this excess is not as dramatic as for second-chance fission. The data of Trufanov *et al.* in Fig. 5(d) appear to have a generally different shape than the present results and evaluations in the $E_n^{\text{out}} \approx 0.6$ –7.0 MeV range, though the observed pre-equilibrium and third-chance-fission features are roughly in line with evaluations. Baryba *et al.* and Boikov *et al.* data in Fig. 5(e) seem to generally agree with the present results as well as the JENDL-5.0 and ENDF/B-VIII.0 evaluations, though JEFF-3.3 shows a notably different shape below $E_n^{\text{out}} \approx 5.0$ MeV suggesting a lower contribution from the third-chance fission process.

Above $E_n^{\text{inc}} = 15.0$ MeV PFNS evaluations generally evolve into a similar shape described by a smoothly increasing PFNS up until $E_n^{\text{out}} = 3.0$ –4.0 MeV, with a large pre-equilibrium peak above that energy. The present results generally support these evaluation results, though as will be seen in Sec. IV D, these similar shapes can produce quite different average neutron energies. Finally, Smirenkin *et al.* data agree well with the present results within uncertainties, considering the large uncertainties in the Li-glass data reported here.

D. Mean PFNS energies

In addition to the shape of the PFNS, the mean PFNS neutron energy is also commonly of interest. The mean PFNS energy ($\langle E \rangle$) results as a function of E_n^{inc} are shown in Fig. 7. Similar conclusions can be made here as were made in comparing PFNS shapes: (1) the onset of second-chance fission, seen here as a drop in the mean PFNS energy near $E_n^{\text{inc}} = 6.0$ –8.0 MeV, is sharper and more dramatic than in the ENDF/B-VIII.0 library, (2) the ENDF/B-VIII.0 result matches the centroid $\langle E \rangle$ value at the minimum of second-chance fission though JEFF-3.3 and JENDL-5.0 also agree within 1–2 σ , and ENDF/B-VIII.0 and JENDL-5.0 agree well with the data above $E_n^{\text{inc}} = 8.0$ MeV with better agreement for JENDL-5.0 than ENDF/B-VIII.0, and (3) there is a general lack of third-chance fission presence in the JEFF-3.3 evaluation compared with the present results and other evaluations.

We also compare to the data of Ethvignot *et al.* [16] for an integration range of $E_n^{\text{out}} = 0.65$ –7.5 MeV in Fig. 8. The results of Ref. [16] were reported almost entirely with regard to the mean energy of the PFNS alone, with a single PFNS spectrum shown for $E_n^{\text{inc}} = 2.1$ –4.0 MeV and with no uncertainties. Interestingly, the results of Ref. [16] are one of very few data sets that did *not* use a measurement of the spontaneous fission PFNS of ^{252}Cf to correct their data for environmental scattering and efficiency effects. Instead, they corrected their PFNS from $E_n^{\text{inc}} = 2.1$ –4.0 MeV with a 1D ratio to match the results of a sixth-order polynomial fit to the data of Boikov *et al.* [9] at $E_n^{\text{inc}} = 2.9$ MeV (see these data

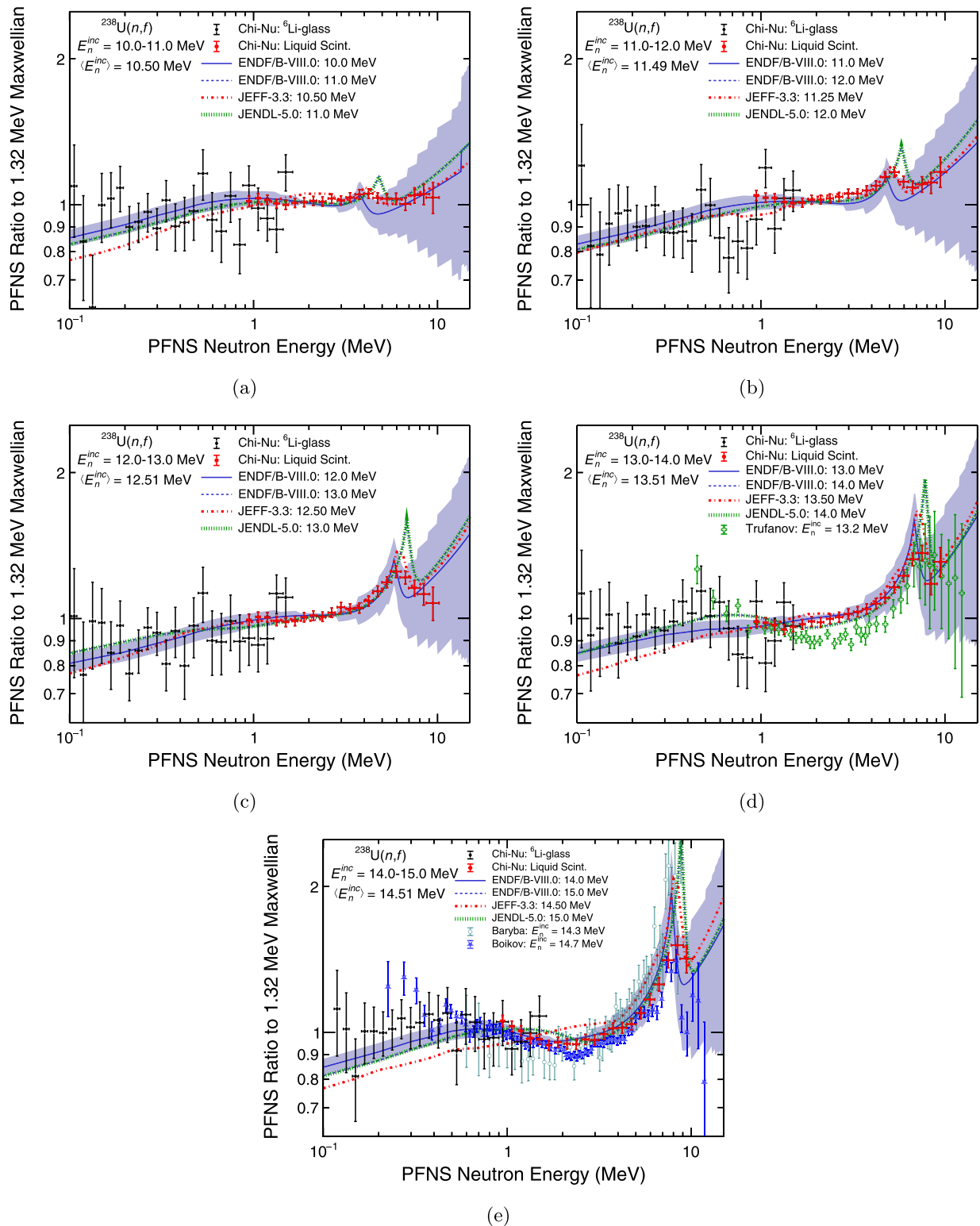


FIG. 5. The present results for Li-glass (black diamonds) and liquid scintillator (red circles) data are shown for (a) $E_n^{\text{inc}} = 10.0\text{--}11.0$, (b) $11.0\text{--}12.0$, (c) $12.0\text{--}13.0$, (d) $13.0\text{--}14.0$, and (e) $14.0\text{--}15.0$ MeV, corresponding to average incident neutron energy, $\langle E_n^{\text{inc}} \rangle$, values of 10.50, 11.49, 12.51, 13.51, and 14.51 MeV, respectively. ENDF/B-VIII.0 [3] evaluations are shown as solid and dashed blue lines, JEFF-3.3 [45] as the dash-dotted red lines, and JENDL-5.0 [46] as dotted green lines. The shaded blue region corresponds to the uncertainty of the lower E_n^{inc} ENDF/BB-VIII.0 evaluation on each plot. All other evaluation uncertainties can be assumed to be similar. Literature data are plotted as compiled in EXFOR [47]. All data are shown as a ratio to a 1.32 MeV Maxwellian distribution.

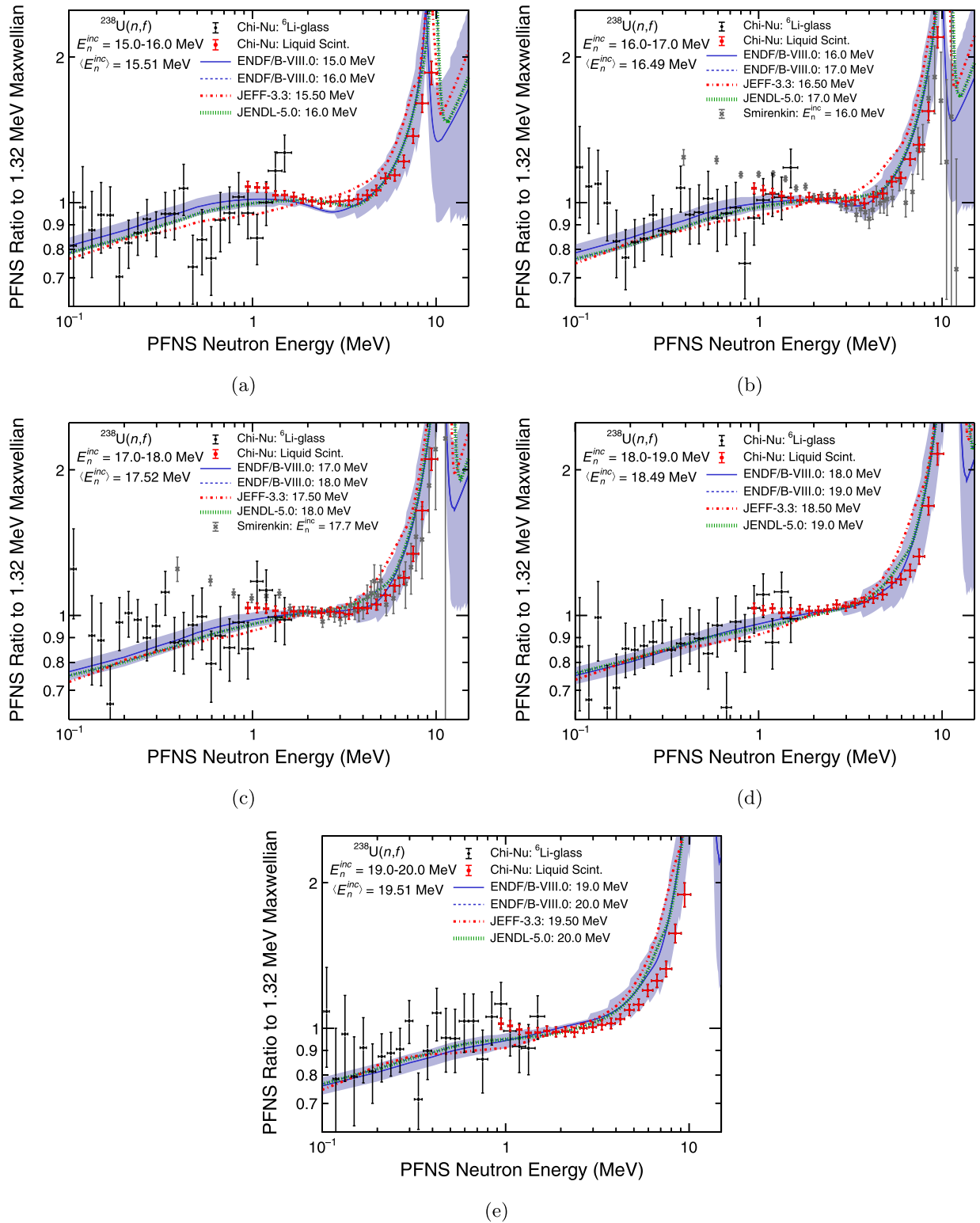


FIG. 6. The present results for Li-glass (black diamonds) and liquid scintillator (red circles) data are shown for (a) $E_n^{inc} = 15.0\text{--}16.0$, (b) $16.0\text{--}17.0$, (c) $17.0\text{--}18.0$, (d) $18.0\text{--}19.0$, and (e) $19.0\text{--}20.0$ MeV, corresponding to average incident neutron energy, $\langle E_n^{inc} \rangle$, values of 15.51, 16.49, 17.52, 18.49, and 19.51 MeV, respectively. ENDF/B-VIII.0 [3] evaluations are shown as solid and dashed blue lines, JEFF-3.3 [45] as the dash-dotted red lines, and JENDL-5.0 [46] as dotted green lines. The shaded blue region corresponds to the uncertainty of the lower E_n^{inc} ENDF/BB-VIII.0 evaluation on each plot. All other evaluation uncertainties can be assumed to be similar. Literature data are plotted as compiled in EXFOR [47]. All data are shown as a ratio to a 1.32 MeV Maxwellian.

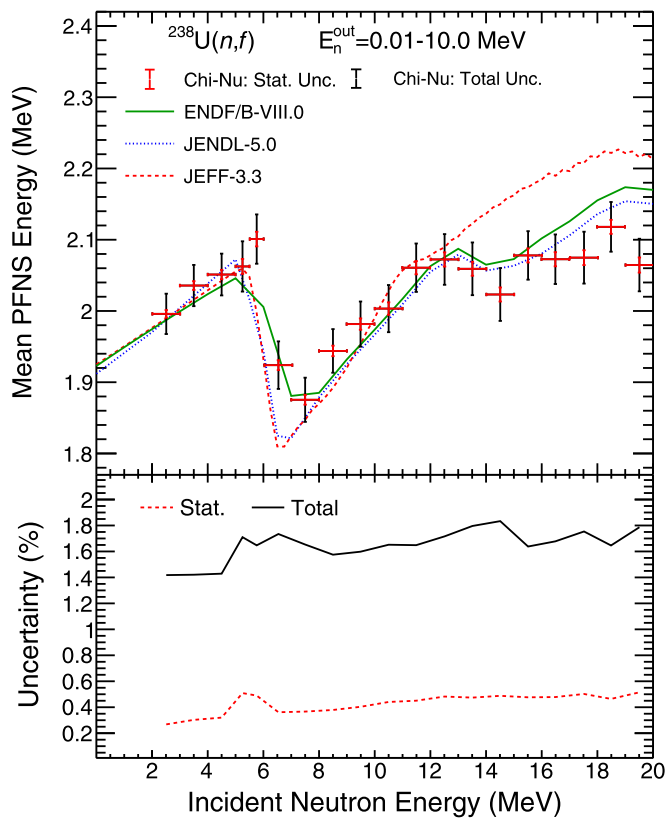


FIG. 7. Mean PFNS energies are a function of E_n^{inc} are shown in the top panel with the total (black) and statistical (red) uncertainties of the data reported here. ENDF/B-VIII.0, JEFF-3.3, and JENDL-5.0 mean energies are shown as the solid green, dashed red, and dotted blue lines, respectively. The trends of total (solid black) and statistical (dashed red) uncertainties of the present results are shown in the bottom panel.

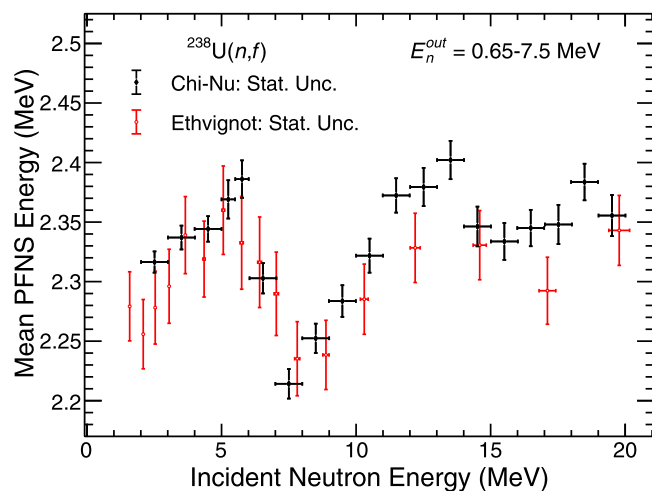


FIG. 8. Comparison of mean PFNS energies from the present results (black diamonds) and those of Ethvignot *et al.* [16] (open, red circles) integrated over the range $E_n^{\text{out}} = 0.65\text{--}7.5$ MeV. Statistical uncertainties are shown for each experiment. See the text for a discussion.

in Fig. 3b), and this 1D efficiency curve was used to correct their data at all other incident energy ranges. The PFNS data of Ref. [16] were also collected at angles of 90, 105, and 120° relative to the incident neutron beam, and so it is expected that the the present results will trend towards higher $\langle E \rangle$ values at higher incident energies where the anisotropic sources like the pre-equilibrium neutron component become important, though even at 90° the measured spectrum is not free of this PFNS component [28].

In general, we see agreement between the present results and those of Ref. [16]. While there may be some evidence for the expected deviations at higher incident energies, both data sets agree within 1–2 σ statistical uncertainty, and would agree well with systematic uncertainties included. Lastly with regard to Ref. [16], there were also $\langle E \rangle$ values reported in the same work over the full E_n^{out} of the PFNS, but (a) these results were heavily based on extrapolation using Watt fits to the data, and (b) the results from those fits yielded uncertainties that are almost an order of magnitude higher than the statistical uncertainties of the results in this work. Thus, we do not compare to these results here.

E. Ratios and systematic trends of Chi-Nu ^{239}Pu , ^{235}U , and ^{238}U PFNS results

Given the consistencies between the ^{238}U experiment described in this article with the ^{239}Pu [21] and ^{235}U [22] measurements by the Ch-Nu team, this collection of results is the first to yield reliable comparisons of all three major actinides across a wide range of incident and outgoing neutron energies. Data for the $^{239}\text{Pu}/^{235}\text{U}$ PFNS ratio are available at $E_n^{\text{inc}} = 1.5$ MeV from Refs. [49,50]. These data were discussed in Ref. [22], and are not shown again here. We also acknowledge the existence of $^{239}\text{Pu}/^{235}\text{U}$ PFNS ratios for nine energy bins from $E_n^{\text{out}} = 1\text{--}10$ MeV and for 1 MeV increments within the range $E_n^{\text{inc}} = 1\text{--}8$ MeV by Noda *et al.* [51]. The only other PFNS ratios available are from Boikov *et al.* [9,10] for $^{235}\text{U}/^{238}\text{U}$, at $E_n^{\text{inc}} = 2.9$ and 14.7 MeV.

Ratios of the PFNS of ^{235}U to ^{238}U for $E_n^{\text{inc}} = 2.0\text{--}3.0$, 7.0–8.0, and 14.0–15.0 MeV are shown in Figs. 9(a)–9(c), including the ratio of data from measurements of Boikov *et al.* [9,10]. The ^{239}Pu -to- ^{238}U PFNS ratios for the same incident energies are shown in Figs. 9(d)–9(f), and for the ^{239}Pu -to- ^{235}U ratio in Figs. 9(g)–9(i). The data of Noda *et al.* [51] are not shown here because the granularity of these data in E_n^{out} is generally too coarse to be informative, and the uncertainty of the ratio data points extends beyond both the upper and lower limits of the y axes of Figs. 9(g)–9(h) in many cases. The covariance of each of these results were propagated through to these ratio results including correlations from data analysis and acquisition processes for these separate experiments. Thus, the total uncertainties on these ratios are dominated by statistical precision, and many systematic effects that could impact each individual measurement are reduced if not eliminated in these ratios.

Focusing first on the ^{235}U -to- ^{238}U PFNS ratios, these isotopes of uranium display very similar PFNS shapes, resulting in experimentally determined PFNS ratios near unity. These ratios also agree well with those of Boikov *et al.* [9,10]

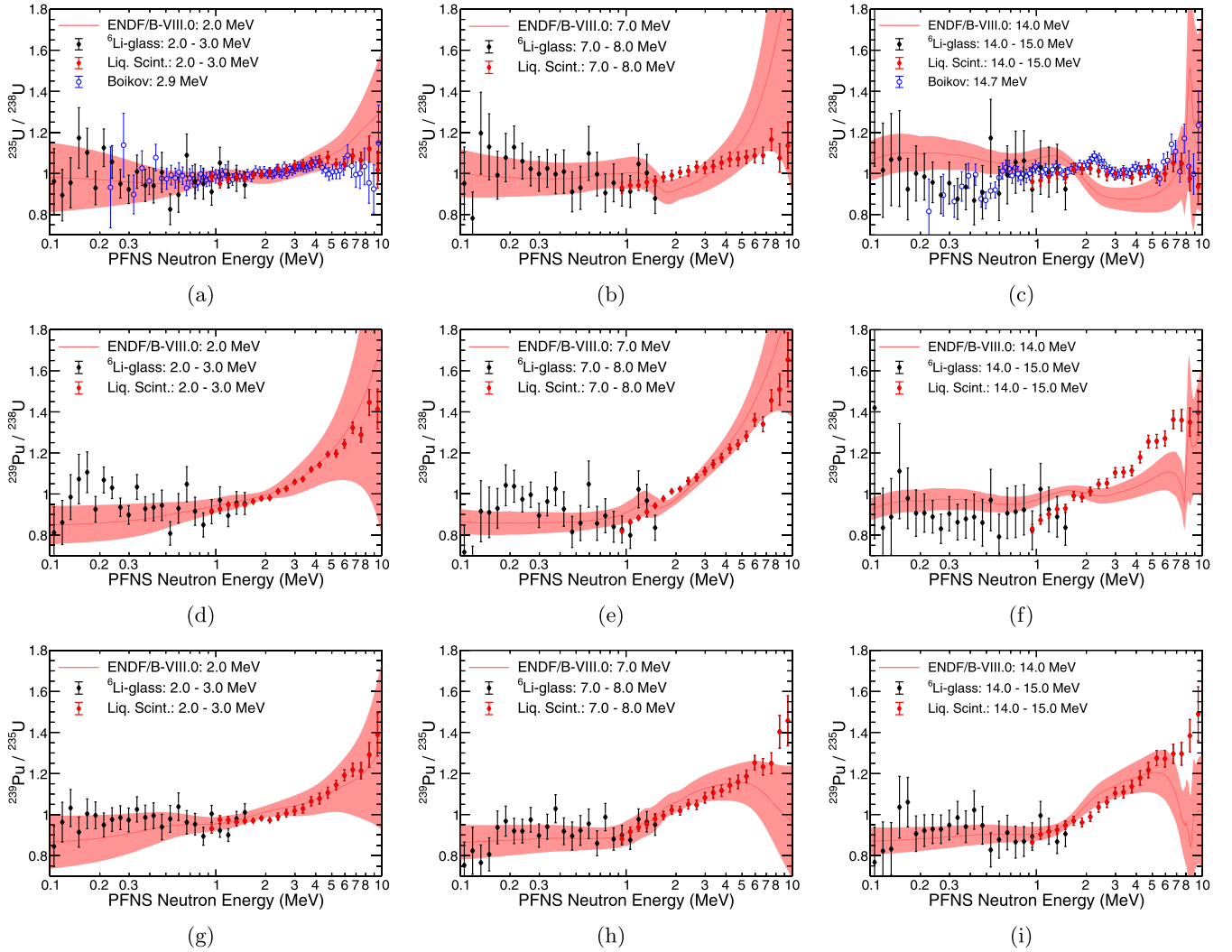


FIG. 9. $^{235}\text{U}/^{238}\text{U}$ PFNS ratios for $E_n^{\text{inc}} =$ (a) 2.0–3.0, (b) 7.0–8.0, and (c) 14.0–15.0 MeV. The $^{239}\text{Pu}/^{238}\text{U}$ ratios for the same E_n^{inc} values are shown (d), (e), and (f), and those for the $^{239}\text{Pu}/^{235}\text{U}$ ratio are shown in (g), (h), and (i), respectively. ENDF/B-VIII.0 evaluation comparisons are shown as the solid red lines, with uncertainties shown as the shaded regions.

in Figs. 9(a) and 9(c). However, the ^{235}U PFNS generally tends to be larger at high E_n^{out} values, and a clear shape variation is observed from $E_n^{\text{out}} = 1.0$ – 1.5 MeV in Fig. 9(c) from differences in the third-chance fission threshold between these nuclei. None of these relatively minor variations are on the level of variation between the ^{235}U and ^{238}U PFNS from the ENDF/B-VIII.0 evaluation, which contains significant structural features from differences in multichance fission and pre-equilibrium components of either PFNS. These features would be smoothed out to an extent with an averaging of the evaluated results over the E_n^{inc} range covered by the Chi-Nu measurements, but the linear interpolation scheme recommended for obtaining intermediate E_n^{inc} values from ENDF/B-VIII.0 (which is the same as recommended for JEFF-3.3 and JENDL-5.0 as well) only averages two distinctly different PFNS shapes at the limits of the E_n^{inc} range of interest. This scheme then yields unphysical PFNS results with multiple multichance fission and pre-equilibrium features in the PFNS, as opposed to the desired smooth distribution averaging over results at each intermediate energy

(see, for example, Figs. 8–11 in Ref. [22]). Lastly, as noted in Ref. [22], the ENDF/B-VIII.0 evaluation of the ^{235}U PFNS tends to be notably larger at high E_n^{out} values than recent experimental measurements, which then yields $^{235}\text{U}/^{238}\text{U}$ PFNS ratios that trend upwards compared with the data in Figs. 9(a)–9(c).

Moving to PFNS ratios with ^{239}Pu in the numerator, the ratios of the ^{239}Pu PFNS to ^{238}U (Figs. 9(d)–9(f)) and to ^{235}U (Figs. 9(g)–9(i)) look broadly quite similar as a result of the general similarity of the ^{235}U and ^{238}U PFNS, and are characterized by a steep increase from $E_n^{\text{out}} = 1.0$ – 10.0 MeV. Variations can be seen in these ratios corresponding again to differences in the threshold and magnitude of multichance fission and pre-equilibrium neutron emission with the overall increasing trend. While these ratios both agree well with ENDF/B-VIII.0 for $E_n^{\text{inc}} = 2.0$ – 3.0 MeV in Figs. 9(d) and 9(g), for the $E_n^{\text{inc}} = 7.0$ – 8.0 MeV the ENDF/B-VIII.0 evaluation of ^{235}U trends higher than the results of Ref. [22] whereas ENDF/B-VIII.0 agrees more closely with the ^{238}U

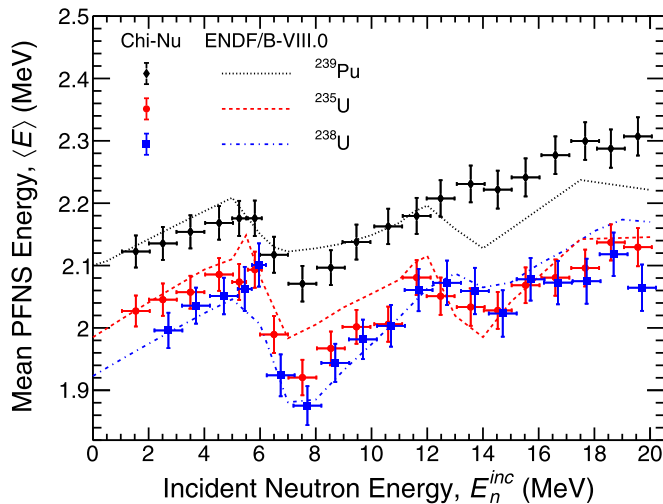


FIG. 10. Mean PFNS energy results from Chi-Nu measurements of the PFNS of ^{239}Pu (black diamonds), ^{235}U (red circles), and ^{238}U (blue squares) are shown here with ENDF/B-VIII.0 results for each of these nuclei shown as the black dotted, red dashed, and blue dash-dotted lines, respectively. Uncertainties shown here are the total uncertainty of each measurement. The ^{238}U data have been shifted up by 0.2 MeV in incident energy to allow the differences between these data and the ^{235}U results to be discerned more clearly.

PFNS results presented in this work, yielding good agreement in Fig. 9(e) but a shape disagreement in Fig. 9(h) especially at the highest E_n^{out} values. Finally, neither of these evaluation ratios for $E_n^{\text{inc}} = 14.0\text{--}15.0$ MeV in Figs. 9(f) and 9(i) reproduce the shape of the data, though the ^{239}Pu -to- ^{235}U ratio in Fig. 9(i) largely agrees within uncertainties of the present results except at the highest energies.

The mean energies from this work and from Refs. [21] and [22] are shown in Fig. 10 with the ENDF/B-VIII.0 evaluation results integrated over the same $E_n^{\text{out}} = 0.01\text{--}10.0$ MeV range covered by the experimental data. Comparisons of each data set to the corresponding evaluations are provided in this work and elsewhere [21,22], so we only comment on the relative features between the different isotopes here. The slope of the average energy trends below thresholds for second-chance fission are fairly similar, with ^{238}U perhaps dropping more sharply than the others extrapolating towards thermal incident energies, and this generally agrees with evaluation results. While ENDF/B-VIII.0 predicts some notable differences for the energy of the second-chance fission threshold and in the placement of the minimum of the second-chance-fission drop in mean PFNS energy, the data suggest less variation between these isotopes for both parameters, though the shape and magnitude of the drop observed in mean PFNS energy does change between isotope with ^{238}U showing the largest drop. Experimental mean energy slopes from $E_n^{\text{inc}} = 7.5\text{--}11.5$ MeV are again quite similar for all three isotopes, above which are clear differences likely from the third-chance fission thresholds and magnitude of the third-chance fission component of the PFNS. A mass-dependent trend may be inferred from the lowest threshold for third-chance fission observed in ^{235}U , followed by ^{238}U and ^{239}Pu , though interestingly the magni-

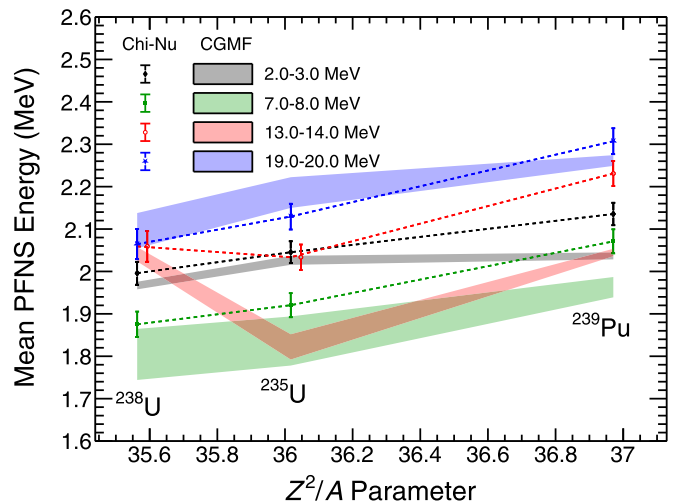


FIG. 11. The mean energy of Chi-Nu results of the PFNS of ^{238}U (left side of figure), ^{235}U (middle), and ^{239}Pu (right) versus the nuclear Z^2/A parameter for incident energy ranges of $E_n^{\text{inc}} = 2.0\text{--}3.0$ (black diamonds), $7.0\text{--}8.0$ (green squares), $13.0\text{--}14.0$ (open, red circles), and $19.0\text{--}20.0$ MeV (blue stars). Data points from the same E_n^{inc} range are connected with dashed lines of the same color to guide the eye. The $E_n^{\text{inc}} = 13.0\text{--}14.0$ MeV data points for ^{238}U and ^{235}U have been shifted by 0.03 along the x axis to avoid overlap with other data. Results from the CGMF [40] code are also shown as the shaded regions of the same color as the Chi-Nu data. The range of the CGMF calculations correspond to the E_n^{inc} ranges shown in the legend.

tude of third-chance fission mean energy variations may track more closely with element identity judging by the fact that ^{235}U and ^{238}U are nearly identical and ^{239}Pu has only a minor impact from this feature. Evaluations were generally poorly guided by the lack of existing experimental data at higher incident energies, resulting in significant differences from the data shown here, though new evaluations are already being performed that include this new experimental guidance.

Similar conclusions to those made above based on Fig. 10 can also be inferred from trends of $\langle E \rangle$ versus the nuclear Z^2/A parameter, where Z is the proton number and A is the mass number. Results for these trends from Chi-Nu measurements of ^{238}U , ^{235}U , and ^{239}Pu are shown in Fig. 11 for $E_n^{\text{inc}} = 2.0\text{--}3.0$, $7.0\text{--}8.0$, $13.0\text{--}14.0$, and $19.0\text{--}20.0$ MeV along with results from the CGMF [40] code for comparison. The Z^2/A parameter was previously considered by Smith *et al.* [52,53] regarding the observed linear relationship of $\langle E \rangle$ versus Z^2/A for the PFNS of ^{233}U , ^{235}U , and ^{239}Pu at $E_n^{\text{inc}} \approx 0.525$ MeV and ^{240}Pu at $E_n^{\text{inc}} \approx 0.85$ MeV, relative to the spontaneous fission PFNS of ^{252}Cf . This quantity is related to the nuclear “fissility” parameter discussed in Ref. [53] and references therein. The results shown in Ref. [52] are not reproduced since Chi-Nu results do not overlap with the E_n^{inc} values for data shown in that work. While we observe a generally trend for almost all E_n^{inc} ranges measured in Chi-Nu experiments, including second-chance fission regions where the PFNS from the fission of each nucleus is changing rapidly with E_n^{inc} , there is a clear divergence from linearity near the third-chance fission threshold (i.e., in the $E_n^{\text{inc}} = 13.0\text{--}14.0$ MeV trend),

where ^{238}U produces a larger $\langle E \rangle$ than ^{235}U . Approximate linearity is regained above this incident energy until $E_n^{\text{inc}} = 20.0$ MeV. Therefore, although the assumption of linearity of $\langle E \rangle$ versus Z^2/A may hold for the PFNS from neutron-induced fission of nuclei at similar E_n^{inc} values, it does not appear to be consistent for all E_n^{inc} , especially near the third-chance fission threshold.

In general, the CGMF code reproduces the Z^2/A trend observation of a significant nonlinearity near the threshold for third-chance fission at $E_n^{\text{inc}} = 13.0\text{--}14.0$ MeV and many $\langle E \rangle$ centroids agree with the Chi-Nu data, though the magnitude of the nonlinearity in CGMF is significantly larger than the data. It is important to note that Hauser-Feshbach fission fragment decay models such as CGMF tend to calculate PFNS distributions with a lower average energy. The cause of this discrepancy is still unknown, and the interplay of many model input parameters like, e.g., fission fragment initial conditions, nuclear structure information, multichance fission probabilities, and more could be contributing. An investigation into this issue is beyond the scope of this work, but comparisons with consistently acquired data sets could potentially give insight into the solution.

V. CONCLUSIONS

The increased interest in development of fast reactor technology has led directly to a need for improvements on experimental measurements of neutron-induced reactions on ^{238}U . Specifically for the PFNS, there has been a series of measurements performed over the last three decades that have guided modern nuclear data evaluations with data spanning incident neutron energies as high as 17.7 MeV, which is rare for any actinide. However, the majority of these measurements were performed by the same experimental team members at the same facility and with similar, if not identical, experimental equipment and analysis procedures. Thus, this collection of literature data is likely correlated, implying that there may be consistent systematic effects common to all of these measurements.

We reported here a measurement of the ^{238}U PFNS from $E_n^{\text{inc}} = 1.5\text{--}20.0$ MeV and from $E_n^{\text{out}} = 0.01\text{--}10.0$ MeV. These measurements were performed at the WNR facility at Los Alamos National Laboratory, and are completely uncorrelated with any all previous measurements of the ^{238}U PFNS. We observe a general agreement with existing literature data, with exceptions of disagreements at the lowest and highest outgoing neutron energies reported from literature data sets, which may suggest a systematic effect across the correlated literature measurements. Both agreements and disagreements are found with the major evaluation libraries ENDF/B-VIII.0, JEFF-3.3, and JENDL-5.0 for various combinations of E_n^{inc} and E_n^{out} . No single evaluation appears to reproduce the com-

plete set of data reported here, but each evaluation is within reasonable agreement considering the precision of the literature data previously available. New evaluations including the reported work are already underway, and should yield higher precision data meeting the needs of the fast reactor communities.

These measurements on ^{238}U are the third in a series of PFNS measurements made by the Chi-Nu collaboration on the major actinides ^{239}Pu , ^{235}U , and ^{238}U , results for which each covered a wide range of incident and outgoing neutron energy with a highly detailed covariance treatment. Given that each measurement was carried out in a nearly identical environment, analyzed with similar techniques, and that the complete covariance of each measurement was calculated and propagated with the correlations between each of these three separate measurements considered, we reported here the first accurate, correlated PFNS ratios of these actinides to each other, and we studied systematic differences in the mean PFNS energies of these isotopes. The ^{235}U and ^{238}U PFNS shapes as a function of incident energy are similar in many respects and ^{239}Pu shows, as expected, an overall higher mean PFNS energy. The differences in magnitude and threshold position of multichance fission features in the mean PFNS energies seem to suggest mass-dependent trends for the third-chance fission threshold, and for third-chance fission component magnitudes (i.e., impact on the mean PFNS energies) that are related to the nuclear proton number. Trends of average PFNS energy to a parameter relating to the nuclear fissility were also seen to support previously observed linear trends, except near thresholds for the third-chance fission process. However, while these results represent an extensive collection of work, further measurements on other nuclei such as ^{240}Pu , ^{233}U , or others are needed to further validate any observational trends proposed here.

ACKNOWLEDGMENTS

This work was supported by the U.S. Department of Energy through Los Alamos National Laboratory and Lawrence Livermore National Laboratory, both of which are operated for the National Nuclear Security Administration of the U.S. Department of Energy (LLNL – Lawrence Livermore National Laboratory, LLC, under Contract No. DE-AC52-07NA27344; LANL – Triad National Security LLC, under Contract No. 89233218CNA000001). This work has benefited from the use of the Los Alamos Neutron Science Center accelerator, LANSCE. We would like to thank F. David Sattler for design work on the Chi-Nu arrays and Mark Chadwick for guidance and discussions. We would also like to acknowledge the contributions of B. Bucher, B. Perdue, T. Bredeweg, M. B. Chadwick, A. Chyzh, E. Kwan, M. Q. Buckner, S. Wender, G. Rusev, M. Jandel, S. Sjue, M. E. Rising, C. J. Solomon, I. Stetcu, and J. Lestone to the Chi-Nu project.

[1] F. Bostelmann, G. Ilas, and W. A. Weiselquist, Oak Ridge National Laboratory Report No. ORNL/TM-2020/1557 (2020).

[2] F. Bostelmann, G. Ilas, and W. A. Weiselquist, *J. Nucl. Engineering* **2**, 345 (2021).

- [3] D. A. Brown, M. B. Chadwick, R. Capote, A. C. Kahler, A. Trkov *et al.*, *Nucl. Data Sheets* **148**, 1 (2018).
- [4] K. Kolos, V. Sobes, R. Vogt, C. E. Romano, M. S. Smith, L. A. Bernstein, D. A. Brown, M. T. Burkey, Y. Danon, M. A. Elsayi, B. L. Goldblum, L. H. Heilbronn, S. L. Hogle, J. Hutchinson, B. Loer, E. A. McCutchan, M. R. Mumpower, E. M. O'Brien, C. Percher, P. N. Peplowski, J. J. Ressler, N. Schunck, N. W. Thompson, A. S. Voyles, W. Wieselquist, and M. Zerkle, *Phys. Rev. Res.* **4**, 021001 (2022).
- [5] R. Capote, Y.-J. Chen, F.-J. Hamsch, N. V. Kornilov, J. P. Lestone *et al.*, *Nucl. Data Sheets* **131**, 1 (2016).
- [6] M. Baba, H. Wakabayashi, M. Ishikawa, N. Nakashima, N. Ito *et al.*, in *Proceedings of a Consultants Meeting on Physics of Neutron Emission in Fission, Mito, Japan*, INDC(NDS)-220 (IAEA, Vienna, 1989), p. 149.
- [7] V. V. Desai, B. K. Nayak, A. Saxena, S. V. Suryanarayana, and R. Capote, *Phys. Rev. C* **92**, 014609 (2015).
- [8] N. V. Kornilov, V. J. Baryba, and O. A. Sal'nikov, All Union Conf. on Neutron Phys., Kiev **3**, 104 (1980).
- [9] G. Boikov, V. Dmitriev, G. Kudyaev, Y. Ostapenko, M. Svirin *et al.*, *Sov. J. Nucl. Phys.* **53**, 572 (1991).
- [10] G. S. Boykov, V. Dmitriev, G. Kudyaev, V. Maslov, Y. Ostapenko *et al.*, *Ann. Nucl. Energy* **21**, 585 (1994).
- [11] A. M. Trufanov, G. N. Lovchikova, M. I. Svirin, A. V. Polyakov, and V. A. Vinogradov, *Phys. At. Nucl.* **64**, 1 (2001).
- [12] G. N. Lovchikova, A. M. Trufanov, M. I. Svirin, V. A. Vinogradov, and A. V. Polyakov, *Phys. At. Nucl.* **67**, 1246 (2004).
- [13] G. N. Smirenkin, G. N. Lovchikova, A. M. Trufanov, M. I. Svirin, and A. V. Polyakov, *Phys. At. Nucl.* **59**, 1865 (1996).
- [14] V. Y. Baryba, V. D. Dmitriev, N. V. Kornilov, and O. A. Sal'nikov, *Sov. Atomic Energy* **43**, 899 (1977).
- [15] V. Y. Baryba, N. V. Kornilov, and O. A. Sal'nikov, Report No. 947, Obninsk, Russia, EXFOR 40740 (1979).
- [16] T. Ethvignot, M. Devlin, R. Drosch, T. Granier, R. C. Haight *et al.*, *Phys. Lett. B* **575**, 221 (2003).
- [17] B. E. Watt, *Phys. Rev.* **87**, 1037 (1952).
- [18] P. Marini, B. Laurent, G. Belier, T. Bonnet, A. Chatillon *et al.*, *EPJ Web Conf.* **193**, 03002 (2018).
- [19] W. Wen, L. Guangwu, and H. Wang, *Ann. Nucl. Energy* **94**, 576 (2016).
- [20] A. Sardet, T. Granier, B. Laurent, and A. Oberstedt, *Phys. Procedia* **47**, 144 (2013).
- [21] K. J. Kelly, M. Devlin, J. M. O'Donnell, J. A. Gomez, D. Neudecker *et al.*, *Phys. Rev. C* **102**, 034615 (2020).
- [22] K. J. Kelly, J. A. Gomez, M. Devlin, J. M. O'Donnell, D. Neudecker *et al.*, *Phys. Rev. C* **105**, 044615 (2022).
- [23] R. C. Haight, H. Y. Lee, T. N. Taddeucci, J. M. O'Donnell, B. A. Perdue *et al.*, *Nucl. Data Sheets* **119**, 205 (2014).
- [24] R. C. Haight, C. Y. Wu, H. Y. Lee, T. N. Taddeucci, B. A. Perdue *et al.*, *Nucl. Data Sheets* **123**, 130 (2015).
- [25] T. N. Taddeucci, R. C. Haight, H. Y. Lee, D. Neudecker, J. M. O'Donnell *et al.*, *Nucl. Data Sheets* **123**, 135 (2015).
- [26] J. M. O'Donnell, *Nucl. Instrum. Methods Phys. Res. A* **805**, 87 (2016).
- [27] M. Devlin, J. A. Gomez, K. J. Kelly, R. C. Haight, J. M. O'Donnell *et al.*, *Nucl. Data Sheets* **148**, 322 (2018).
- [28] K. J. Kelly, T. Kawano, J. M. O'Donnell, J. A. Gomez, M. Devlin *et al.*, *Phys. Rev. Lett.* **122**, 072503 (2019).
- [29] K. J. Kelly, P. Marini, J. Taieb, M. Devlin, D. Neudecker *et al.*, *Nucl. Data Sheets* **173**, 42 (2021).
- [30] K. J. Kelly, M. Devlin, J. M. O'Donnell, D. Neudecker, and E. A. Bennett, *Nucl. Instrum. Methods Phys. Res. A* **1010**, 165552 (2021).
- [31] K. J. Kelly, J. M. O'Donnell, J. A. Gomez, M. Devlin, and E. A. Bennett, *Nucl. Instrum. Methods Phys. Res. A* **1045**, 167531 (2023).
- [32] P. W. Lisowski and K. F. Schoenberg, *Nucl. Instrum. Methods Phys. Res. A* **562**, 910 (2006).
- [33] C. Y. Wu, R. A. Henderson, R. C. Haight, H. Y. Lee, T. N. Taddeucci *et al.*, *Nucl. Instrum. Methods Phys. Res. A* **794**, 76 (2015).
- [34] H. Y. Lee, T. N. Taddeucci, R. C. Haight, T. A. Bredeweg, A. Chyzh *et al.*, *Nucl. Instrum. Methods Phys. Res. A* **703**, 213 (2013).
- [35] K. J. Kelly, J. A. Gomez, J. M. O'Donnell, M. Devlin, R. C. Haight *et al.*, *Proceedings of the 20th Topical Meeting of the Radiation Protection and Shielding Division, Santa Fe, NM* (American Nuclear Society, Illinois, 2018).
- [36] K. J. Kelly, M. Devlin, J. M. O'Donnell, and E. A. Bennett, *Phys. Rev. C* **104**, 064614 (2021).
- [37] G. Knoll, *Radiation Detection and Measurements* (John Wiley and Sons, New York, 1996).
- [38] C. J. Werner, J. Armstrong, F. B. Brown, J. S. Bull, L. Casswell *et al.*, LA-UR-17-29981 (2017).
- [39] C. J. Solomon, C. Bates, and J. Kulesza, LA-UR-17-21779, March 30, Los Alamos, 2017.
- [40] P. Talou, I. Stetcu, P. Jaffke, M. E. Rising, A. E. Lovell, and T. Kawano, *Comput. Phys. Commun.* **269**, 108087 (2021).
- [41] J. E. Simmons and R. L. Henkel, *Phys. Rev.* **120**, 198 (1960).
- [42] A. S. Vorobyev, A. M. Gagarski, O. A. Shcherbakov, L. A. Vaishene, and A. L. Barabanov, *JTEP Lett.* **102**, 203 (2015).
- [43] A. S. Vorobyev, A. M. Gagarski, O. A. Shcherbakov, L. A. Vaishene, and A. L. Barabanov, *JTEP Lett.* **107**, 521 (2018).
- [44] A. E. Lovell, P. Talou, I. Stetcu, and K. J. Kelly, *Phys. Rev. C* **102**, 024621 (2020).
- [45] A. J. Plompen, O. Cabellos, C. De Saint Jean, M. Fleming, A. Algora *et al.*, *Eur. Phys. J.* **56**, 181 (2020).
- [46] K. Shibata, O. Iwamoto, T. Nakagawa, N. Iwamoto, A. Ichihara *et al.*, *J. Nucl. Sci. Techn.* **48**, 1 (2011).
- [47] V. V. Zerkov and B. Pritychenko, *Nucl. Instrum. Methods Phys. Res. A* **888**, 31 (2018).
- [48] D. Neudecker, R. Capote, D. L. Smith, T. Burr, and P. Talou, *Nucl. Sci. Eng.* **179**, 381 (2015).
- [49] J. P. Lestone and E. F. Shores, *Nucl. Data Sheets* **119**, 213 (2014).
- [50] M. Sugimoto, A. B. Smith, and P. T. Guenther, *Nucl. Sci. Eng.* **97**, 235 (1987).
- [51] S. Noda, R. C. Haight, R. O. Nelson, M. Devlin, J. M. O'Donnell *et al.*, *Phys. Rev. C* **83**, 034604 (2011).
- [52] A. Smith, P. T. Guenther, G. Winkler, and R. McKnight, *Nucl. Sci. Eng.* **76**, 357 (1980).
- [53] D. N. Poenaru, R. A. Gherghescu, and W. Greiner, *Rom. Rep. Phys.* **63**, 1133 (2011).